Calculated Viscous and Scale Effects on Transonic Aeroelasticty

John W. Edwards*

NASA Langley Research Center, Hampton, Virginia 23681-2199

A viscous–inviscid interactive coupling method is used for the computation of unsteady transonic flows. A lag-entrainment integral boundary layer method is used with a transonic small-disturbance potential code to compute the transonic aeroelastic response for two wing flutter models. By varying the modeled length scale, viscous effects may be studied as the Reynolds number per reference chord length varies. Appropriate variation of modeled frequencies and generalized masses then allows comparison of responses for varying scales or Reynolds number. Two wing flutter models are studied: one a 4% thick swept wing and the other a transport aircraft wing. Calculations for both wings show limit cycle oscillation behavior at transonic speeds in the vicinity of minimum flutter speed indices with amplitudes which are affected by Reynolds number.

Nomenclature

A, B, E_1, F, G_1, H_1	=	constants in variable expressions
c	=	wing root chord length
e	=	error between viscous and inviscid u velocities at the edge of the boundary layer
f_i	=	variable expressions
H	=	boundary layer displacement shape factor
$\bar{H}$	=	boundary layer compressible shape factor
K_δ	=	displacement thickness integrator gain constant
$K_1(\delta^*)$	=	displacement thickness integrator variable gain
M	=	Mach number
$\bar{m} = \rho u \delta^*$	=	boundary layer mass flow rate
Q_f	=	dynamic pressure at flutter, psi
Re	=	Reynolds number per root chord length
s	=	Laplace transform variable
t'	=	Ut/c, nondimensional time
t	=	time, s
u	=	perturbation velocity component in x direction
x, y, z	=	nondimensional Cartesian coordinates
z_{tip}	=	wing tip, trailing-edge displacement, in.
$\bar{z}_{\text{tip}}$	=	z_{tip}/λ_l, scaled wing tip, trailing-edge displacement
δ^*	=	boundary layer displacement thickness
Θ	=	boundary layer momentum thickness
λ_l	=	l_m/l_{ac}, model to aircraft length ratio
$\lambda_{(.)}$	=	flutter model scale factors in Table 1
ρ	=	gas density
ϕ	=	nondimensional perturbation velocity potential
ω_f/ω_α	=	ratio of wing flutter frequency to first torsion mode frequency

Subscript

e	=	boundary layer edge

Superscripts

i	=	"outer" inviscid flow
v	=	"inner" viscous flow

Introduction

THE onset of transonic shock-induced flow separation is known to be associated with a variety of nonclassical aeroelastic instability and response phenomena [1–13] variously referred to as single degree of freedom flutter, limited amplitude flutter, limit cycle oscillations (LCO), control surface buzz, shock-induced oscillations (SIO), and buffeting. A characteristic of the "instabilities" involved is a tendency to grow to a constant or bounded "limit amplitude" which can vary from a nuisance level to levels large enough to cause structural failure. In the latter case, the nonclassical response, generically referred to herein as LCO, is typically observed near the flutter boundary, making a distinction between the two response mechanisms difficult. Edwards and Malone [14] and Edwards [15] reviewed these features of transonic aeroelasticity, concluding that 1) computational capability for such cases would require modeling of dynamically separating and reattaching viscous boundary layers and 2) such capability was then not yet mature for wings or more complete configurations.

Interactive boundary layer modeling (IBLM) provides an alternative to such direct computation of flows involving viscous shear layers. Separate computations are made for an inner viscous boundary layer region and an outer inviscid flow region as illustrated in Fig. 1. The velocity component in the freestream direction is u. Subscript e denotes the edge of the boundary layer, while superscripts i and v denote inviscid and viscous variables. Green et al. [16] developed an integral boundary layer lag-entrainment method to compute displacement thickness δ^*, which was used to update the flow tangency boundary condition of the inviscid solver. This "direct" solution method for the entrainment equation becomes singular at flow separation and "inverse" computation methods [17–22] have been developed in attempts to treat flow separation.

Edwards [23] summarized developments of such inverse computational methods by many authors [17–22,24–31] and extended the inverse method of Howlett [30] with a then-new interactive viscous–inviscid coupling procedure capable of treating transonic shock-induced separation and reattachment of unsteady flows about airfoils. The method was implemented in the Computational Aeroelasticity Program—Transonic Small Disturbance (CAP-TSD) code [32,33] and provided the first numerical

Table 1　Mach scaling used for flutter model testing

Parameter	Symbol	Ratio—model/aircraft
Length	λ_l	l_m/l_{ac}
Density	λ_ρ	ρ_m/ρ_{ac}
Velocity	λ_V	V_m/V_{ac}
Mass	λ_m	$\lambda_m \lambda_l^3$
Frequency	λ_f	λ_V/λ_l
Force	λ_F	$\lambda_\rho \lambda_V^2 \lambda_l^2$
Torque	λ_T	$\lambda_\rho \lambda_V^2 \lambda_l^3$
Dynamic pressure	λ_q	$\lambda_\rho \lambda_V^2$
Reynolds no.	λ_{Re}	$\lambda_\rho \lambda_V \lambda_l \mu_{ac}/\mu_l$

computation of the experimentally observed hysteresis in a Mach number of transonic SIO about the 18% thick circular arc airfoil. The method was further extended in the CAP-TSDV code [34] to enable viscous treatment of wings ("V" signifying the stripwise implementation of the viscous boundary layer model). Applications are given of transonic flutter and LCO for two wing flutter models. Bartels [12] and Bartels and Rothmayer [13] developed an IBLM with a fully unsteady finite-difference boundary layer model interacted with a two-dimensional TSD code and presented many SIO calculations. Dreim et al. [35] present results using the CAP-TSDV code of LCO behavior observed on the B-2 bomber. Huttsell et al. [36] present results from this code and from a higher order Reynolds averaged Navier–Stokes code of wing-control surface buzz. More recent computations of LCO with the CAP-TSDV code are given in [37,38] while alternative computational methodologies for computation of LCO behavior are given in [39,40].

In this paper, calculations of wing flutter are presented for two cases: a 4% thick swept wing flutter model [34], and a thicker transport aircraft wing flutter model [41]. Viscous effects are shown for both models, including examples of LCO. The effect of model scale, and thus Reynolds number, is studied for both models. Evidence of a significant effect of Reynolds number for flutter and LCO conditions involving separation onset is shown.

Mathematical Method

Details of the inviscid flow equation, the boundary layer equations, the modifications to boundary conditions, and the IBLM coupling procedure are summarized in this section. Further details are given in [23,34].
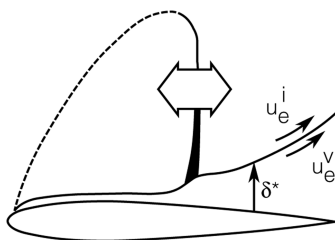
Inviscid Flow Equation

The CAP-TSD potential equation code is used in this analysis. The CAP-TSD code uses an approximate factorization algorithm for a time-accurate solution of the unsteady TSD equation [31,32]

$$\frac{\partial f_0}{\partial t} + \frac{\partial f_1}{\partial x} + \frac{\partial f_2}{\partial y} + \frac{\partial f_3}{\partial z} = 0$$

with

$$f_0 = -A\phi_t - B\phi_x \qquad f_1 = E_1\phi_x + F_1\phi_x^2 + G_1\phi_y$$
$$f_2 = \phi_y + H_1\phi_x\phi_y \qquad f_3 = \phi_z$$

where ϕ is the inviscid-disturbance velocity potential and $A = M^2$, $B = 2M^2$, $E_1 = 1 - M^2$, $F = -\frac{1}{2}[3 - (2 - \gamma)]M^2$, $G_1 = -\frac{1}{2}M^2$,

Fig. 1　Sketch of shock-boundary layer interaction.

and $H_1 = -M^2$. The Mach number is M and the ratio of specific heats is γ. For the 2-D version of the code $f_2 = G_1 = 0$. The code contains modifications to these coefficients developed by Batina [42] to approximate the effects of shock generated entropy and vorticity.

Lag-Entrainment Boundary Layer Equations

The effect of a turbulent viscous boundary layer is modeled in the quasi-steady manner of Green et al. [16] by solving a set of ordinary differential equations, termed the boundary layer equations (BLE), for the integral boundary layer quantities: momentum thickness θ, shape factor $\bar{H}$, and entrainment coefficient C_E. The various closure parameters in these equations are given in [30]. In this form, the equations are suitable for attached flow boundary layers and provide the boundary layer displacement thickness

$$\delta^* = H\theta$$

This provides a direct calculation of the viscous modification to the airfoil shape to be implemented in the boundary conditions as discussed in [34].

At separation, the equations become singular and an alternative inverse IBLM is used as described by Howlett [30], Melnik and Brook [18], and LeBalleur and Girodroux-Lavigne [19]. In this form, the equation for θ is replaced by an equation for the viscous edge velocity u_e^v, and θ and δ^* are obtained from the interactive boundary layer coupling method described next.

Numerical Implementation

From the leading edge of the airfoil, the boundary layer is approximated by the turbulent boundary layer on a flat plate. At a specified point, numerical integration of the inverse boundary layer equations is implemented with a fourth-order Runge–Kutta method. For the Mach number range studied, it was found that the inverse equations, in conjunction with the coupling method described next, converged rapidly for attached flow upstream of regions of flow separation (and also for downstream regions of reattached flow). This obviated the use of the direct boundary layer equations, thus circumventing the numerically troublesome switching between the direct and inverse equations in separating flow regions, where the largest parameter gradients occur.

Interactive Boundary Layer Coupling Method

Because the intended applications of the IBLM include cases of wing flutter, including SIO and LCO, the coupling method was developed based on the observation that at the transonic flow conditions of interest, the flowfield is frequently inherently unsteady, displaying oscillating shocks and separating and reattaching boundary layers. The interacting boundary layer method is thus regarded as a simulation of two dynamic systems, the outer inviscid flow and the inner viscous flow, whose coupling requires active control elements to minimize the coupling error between the two systems. The elements used, illustrated in analog block diagram fashion in Fig. 2, include a variable gain integral control element for the displacement thickness and a first-order smoothing filter for the momentum thickness estimate [23,34]. In Fig. 2 s is the Laplace transform variable, a is the lag constant in the momentum smoothing filter, the mass flow parameter is $\bar{m} = \rho_e^i u_e^i \delta^*$, and $\hat{\Theta}$ is the smoothed momentum thickness. The input to the integral control element is the error in the boundary layer edge velocity $e(x) = u_e^v(x) - u_e^i(x)$. Finally, K_δ and $K_1(\delta^*)$ are constant and variable gains.

For the 3-D code, the boundary layer and interactive coupling equations are solved independently at each spanwise chord station on the wing. This is accomplished at each time step, within the Newton linearization iteration loop of the approximate factorization solution algorithm of the resulting CAP-TSDV code, where the appended V indicates the IBLM capability.
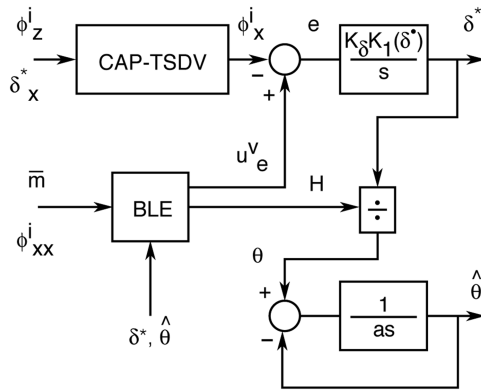
Fig. 2 Schematic diagram of variable gain, integral control, and viscous–inviscid interative coupling method.

Fig. 3 Planview of AGARD Wing 445.6 standard aeroelastic configuration.

Scaling and Reynolds Number Modeling

The scaling relations used for flutter models, referred to as Mach scaling [43,44], are given in Table 1. In constructing a flutter model, all of the scaling parameters $\lambda_{(\cdot)}$ must be considered. The situation for a computational simulation of Reynolds number effect is much simpler, because there are no constraints on "model" size. Assuming the simulated model responses are to be computed for the same gas, same Mach number, same dynamic pressure, and same relative deflections, we have $\lambda_\rho = \lambda_V = \lambda_q = 1$, leaving the following scaling relations for computational aeroelasticity:

generalized masses:

$$\lambda_m = \lambda_l^3$$

modal frequencies:

$$\lambda_f = \lambda_l^{-1}$$

Reynolds number per root chord:

$$\lambda_{Re} = \lambda_l$$

In cases such as the present, where experimental data from actual wind-tunnel models are available and we wish to predict the behavior of a larger flight vehicle, the roles of "aircraft" and model in the scaling relations are reversed. For example, if we wish to predict computationally the response of a flight vehicle 20 times larger than the flutter model, the computational aeroelastic analysis should be performed by modifying the aeroelastic equations of motion of the flutter model with $\lambda_l = 20$, $\lambda_m = 8000$, $\lambda_f = 0.05$, and $\lambda_{Re} = 20$. That is, generalized masses are increased by λ_l^3, modal frequencies are decreased by λ_l, and the Reynolds number increased by λ_l. The procedure for studying the effects of scale or Reynolds number on, for example, flutter, is thus, determine the computational aeroelastic modal root loci for the two length scales (i.e., modal frequencies and dampings versus dynamic pressure); and then, compare the scaled frequency $\lambda_l \omega_f$ and damping ς, with those obtained from flutter model tests or computation with $\lambda_l = 1$. Also amplitude effects such as wingtip motion can be compared using the scaled deflection $\bar{z}_{tip} = z_{tip}/\lambda_l$.

Model Descriptions and Results

Wing Flutter Models

The first wing flutter model, shown in Fig. 3, is the AGARD standard aeroelastic configuration [45,46], which was tested in the Transonic Dynamics Tunnel (TDT) at NASA Langley Research Center. It is a semispan wall-mounted model having a quarter-chord sweep angle of 45 deg, a panel aspect ratio of 1.65, and a taper ratio of 0.66. The wing had a NACA 65A004 airfoil section and was constructed of laminated mahogany. The wing is modeled structurally using the first four natural vibration modes, with natural frequencies ranging from 9.6 Hz for the first bending mode to 91.54 Hz for the second torsion mode. The CAP-TSDV calculations
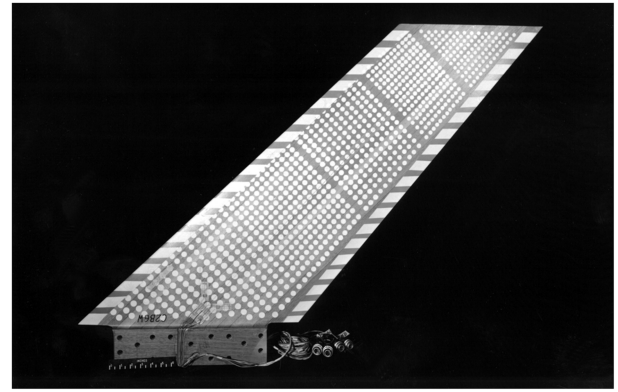
were performed on a $150 \times 30 \times 80$ point computational grid with 100 points along each of 15 spanwise chords on the wing. Other computational conditions were nondimensional time step $dt = 0.05$, one Newton iteration, and $K_\delta = 0.00030$.

The second wing flutter model, shown in Fig. 4, is a transport aircraft wing configuration also tested in the TDT. The semispan wing-fuselage model was mounted on the wind-tunnel sidewall and tested in air, with experimental flutter data obtained for Mach numbers from 0.628 to 0.888. The wing has a taper ratio of 0.29 and a midchord sweep of 23 deg. The airfoil thickness varies from 13% at the symmetry plane (for the extended wing-alone configuration analyzed) to 8.5% at the wing tip. Six natural vibration modes were included in the calculations, with frequencies ranging from 4.3 to 62.7 Hz. The CAP-TSDV calculations were performed on a $100 \times 50 \times 80$ point computational grid with 45 points along each of 33 spanwise chords on the wing. Other computational conditions were nondimensional time step $dt = 0.03$, one Newton iteration, and $K_\delta = 0.00010$.

AGARD Wing 445.6 Flutter Calculations

The majority of published calculations for this model (actually a series of models with similar planforms) are for the "weakened model no. 3" tested in air, because this test covered the largest transonic speed range and showed a significant transonic dip effect. Edwards [34] summarizes a number of these calculations from both inviscid and viscous methods. Many authors have reported flutter calculations for this model in very good agreement with those given in [34] and with experiment for the subsonic flutter points. A small but significant improvement in agreement with the experimental flutter speed index is shown in [34] for the CAP-TSDV result versus the inviscid CAP-TSD result. There is an unresolved disparity for the two low supersonic flutter points with the consensus of the computed flutter speed indices (both inviscid and viscous) being significantly
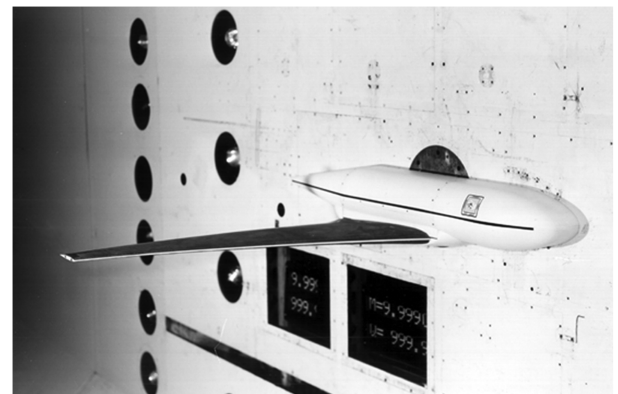

Fig. 4 Transport aircraft wing flutter model mounted in the NASA Langley Transonic Dynamics Tunnel.

higher than experiment. The focus upon this case is unfortunate in that the model tested in air resulted in unrealistically large mass ratios and small reduced flutter frequencies. In addition, there are no strong transonic or viscous effects at the experimental flutter conditions reported for this model. Even for the $M = 0.96$ condition there are no strong shocks on the wing and the boundary layer remains fully attached.

Models Tested in Heavy Gas: It is thus desirable to study results for the weakened models nos. 5 and 6 which were tested in heavy gas and had more reasonable ranges of mass ratio and frequency. CAP-TSDV calculations for these cases are shown in Fig. 5. Again, for these cases with $M \leq 1.0$, the CAP-TSDV results are in excellent agreement with experiment for $M = 0.74$ and 0.92. Because of issues with experimental flutter testing very near $M \sim 1.0$, calculations have not been attempted for the third experimental flutter point at that Mach number. Instead, calculations at $M = 0.90–0.96$ revealed an interesting minimum feature in the flutter speed index parameter at $M = 0.95$. Figure 6 shows flutter boundaries for five values of the scale factor λ_l, ranging from 1 to 40 and covering Reynolds number per root chord from 3.5×10^6 to 140×10^6. Insets show typical time histories for converging and diverging responses from which the stability boundaries were determined. For all the values of λ_l there is a minimum flutter speed index near $M = 0.95$ seen in the faired curves connecting the data points. For Mach numbers below this minimum, there is a small, monotonic decrease in flutter speed index with increasing Reynolds number. The amount of the decrease is less than 1%. At $M = 0.94$ and 0.96 there is a reversal of this trend, with the flutter speed index for $\lambda = 40$ increasing over that for $\lambda = 20$.

Further numerical experimentation at $M = 0.96$ revealed interesting nonlinear response features. It was found that the estimated damping of the flutter mode was dependent upon the amplitude of the response time history. Figure 7 shows two instances
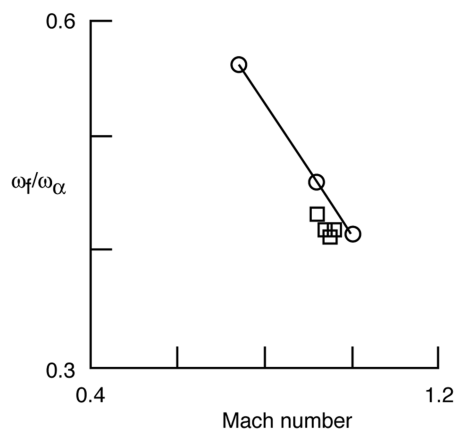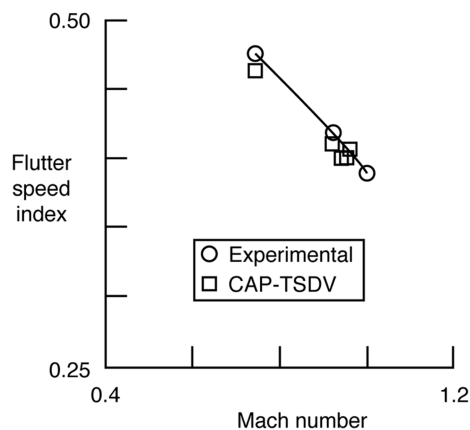
of this behavior on the "backside" of this transonic dip in the flutter boundary for λ_ls of 1 and 40. In each case, stability boundaries inferred from responses with larger amplitudes of motion lead to lower flutter speed index values. Such amplitude dependent stability behavior is an indication that nonlinear processes are involved, and that nonlinear response mechanisms, such as limit cycle oscillations may be anticipated. This was investigated by calculating a simulated wing "tip rap" response for $M = 0.96$ and $Q = 0.75$ psi, shown in Fig. 8. The interpolated flutter dynamic pressure from the experimental data for this Mach number is $Q_f = 0.757$ psi. The early portion of the response indicates positive damping of the flutter mode and also a higher frequency mode. The damping of the flutter mode decreases as the response amplitude decays to approximately 0.12 in. peak to peak, where stable limit cycle oscillations persist.

This limit cycle behavior was further studied by sequentially increasing the dynamic pressure between computed runs from $Q = 0.5$ to 0.81 psi. The resulting tip deflection time history is shown in Fig. 9. Twelve sequential computer runs with a total of 24,000 time steps are shown. The dynamic pressure was incremented as indicated in steps between restarted runs. For $Q \leq 0.60$ psi, the response is damped and for $Q = 0.70$ psi, small neutrally stable oscillations are seen. With Q increased to 0.78 psi, slowly divergent oscillations develop and with further increase to 0.81 psi, the divergent oscillations grow with increased negative damping until the amplitude reaches approximately 0.12 in. peak to peak. The growth of the oscillations then quenches and it appears that a limit cycle condition will again develop, although further calculations are needed to fully establish this feature.
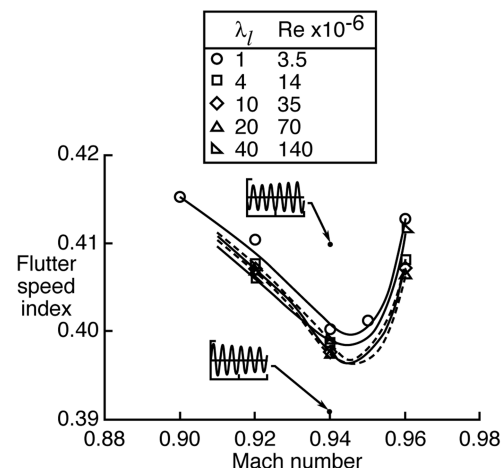

Fig. 6 Calculated effect of Reynolds number on flutter near minimum transonic flutter speed.

Fig. 5 Comparison between experimental and calculated flutter speed index and frequency for the AGARD Wing 445.6 tested in heavy gas.
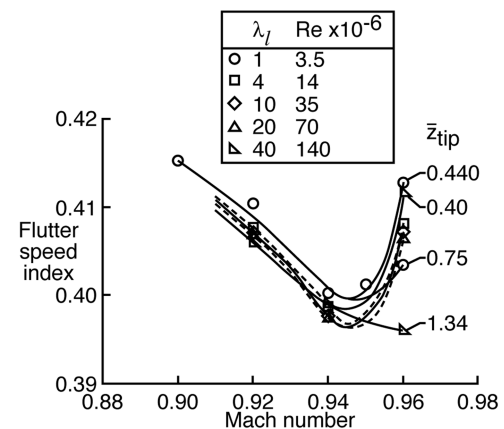

Fig. 7 Calculated effect of motion amplitude upon flutter boundary near minimum transonic flutter speeds.
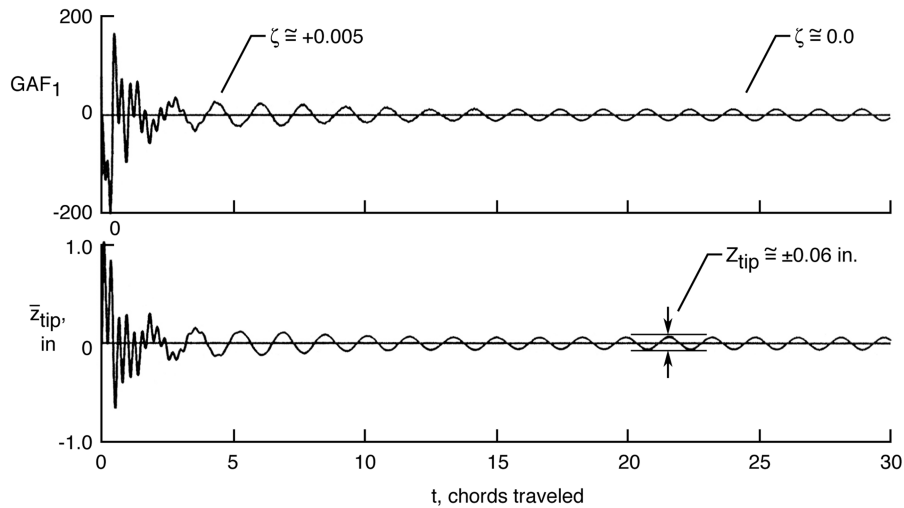
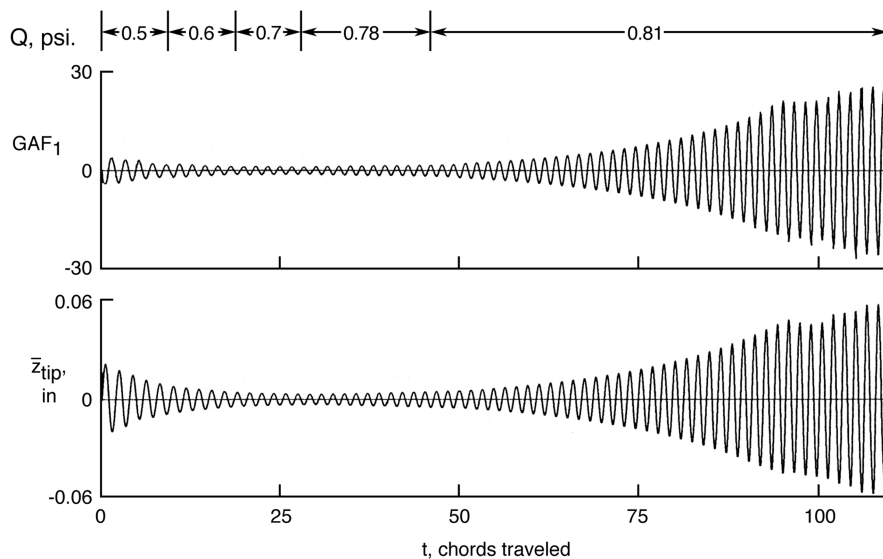Fig. 8   Calculated AGARD Wing 445.6 tip response in heavy gas for $M = 0.96$ and $Q = 0.75$ psi.

Fig. 9   Calculated AGARD Wing 445.6 response in heavy gas for $M = 0.96$ and increasing dynamic pressure; $\lambda_l = 1$.

This same sequence of increasing dynamic pressure calculations was performed for $\lambda_l = 10$, or $Re = 35 \times 10^6$, and the results are shown in Fig. 10. A very similar behavior is shown in Fig. 9 for $\lambda_l = 1$ and $Re = 35 \times 10^6$. Hence, for this wing geometry and "test" conditions, the nonlinear effect of motion amplitude dominates the effect of Reynolds number.

This limit cycle behavior for this model was only observed for the highest calculated Mach number $M = 0.96$, which lies on the backside of the small transonic dip seen in Fig. 5. At this Mach number and for the wing motions calculated, the flow is fully attached with no significant transonic features. The boundary layer coupling method performed well, with well-converged displacement thickness profiles. Numerical flow visualizations of the wing pressure showed details which are possibly key to this nonlinear response behavior. At this Mach number and for this thin wing, significant regions of near sonic flow develop adjacent to the wing upper and lower surfaces as the wing oscillates. Very high frequency upstream moving pressure waves are seen in the visualizations which are consistent with forward propagating Mach waves. At a given point on the wing, the frequency of these pressure waves is 10–20 times the flutter mode frequency for this case. The amplitude of these calculated limit cycles is small and no mention of such behavior is reported [46]. It is unlikely that such small motions, even if present, would have been detected because they would have been heavily masked by the model response to tunnel turbulence.

One final computational experiment for this case involved perturbing the LCO obtained at the end of the sequence shown in Fig. 10. Figure 11 shows this result obtained by restarting from the last sequence with all modal displacements and velocities doubled. Instead of returning to the original LCO state, the response slowly diverges to more than 5 times the original amplitude. Again, further calculations are needed to establish the final state of the system.

Transport Wing Flutter Calculations

The transport wing flutter model shown in Fig. 4 was tested in the Transonic Dynamics Tunnel at NASA Langley Research Center. Gibbons [41] presents flutter calculations for the model including spatial and temporal convergence studies, and surface pressure coefficient comparisons for rigid and statically deformed cases, using TSD, Euler, and Navier–Stokes methods. For the present study, the effects of including viscous effects and varying Reynolds number by varying the model scale were investigated using the CAP-TSDV code.

Wind-Tunnel Model Scale, $\lambda_l = 1$: The model was constructed from a stepped-thickness aluminum plate with end-grain balsa wood providing the airfoil contour. The wing was mounted low on the sidewall mounted fuselage model which had a circular cross section with a conical aft end. The wing root angle of attack was varied during the test to minimize loading on the wing. The maximum angle
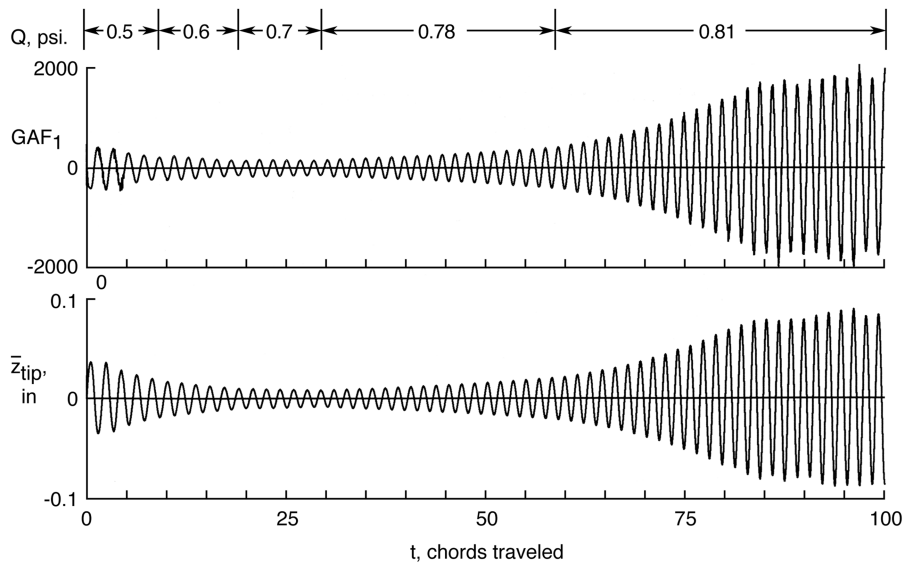
Fig. 10 Calculated scaled AGARD Wing 445.6 response in heavy gas for $M = 0.96$ and increasing dynamic pressure; $\lambda_l = 10$.

needed for this purpose was 0.2 deg at the highest tested Mach number. This root angle was used for the calculations described next. This resulted in calculated static tip deflections (for $\lambda_l = 1$) of -1.33 in. at $M = 0.628$ and $+1.35$ in. at $M = 0.888$. The Reynolds numbers for these two Mach numbers were 2.17×10^6 and 1.14×10^6, respectively, based on the 2.0-ft root chord. The model had a 4.4 ft. semispan.

Contour plots of the upper and lower wing surface pressure, displacement thickness, and skin friction are shown in Fig. 12 for
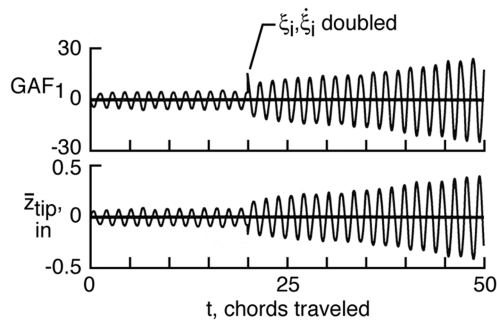

Fig. 11 Effect of perturbation from limit cycle oscillation condition; $M = 0.96$, $\lambda_l = 10$, $Q = 0.81$ psi, heavy gas.

$M = 0.888$. Note the lower surface leading-edge suction peak and mild inboard shock seen in the pressures. The lower surface displacement thickness is similar to the upper surface with maximum thicknesses below 1% except near the root where the lower surface shock produces a thickness of approximately 1.5% root chord. The skin friction reflects these features seen in the displacement thickness and is informative regarding closeness to separation. The lower surface trailing edge is separated at the root and there is a small separation bubble just inboard of the tip and aft of the leading-edge suction peak. The skin friction coefficient is low in the trailing-edge region of the upper surface, reaching a minimum near 88% span. This region and the upper surface separation bubble are key in the effect of amplitude upon flutter mode response described next.

Calculated flutter speed indices and frequencies versus Mach number are compared with experiment in Fig. 13. The linear CAP-TSD, Euler, and Navier–Stokes results are from Gibbons [41] while the four CAP-TSDV data points are new. Comparison of these flutter boundaries leads to similar observations as for the 445.6 wing:

1) Inviscid calculations agree among themselves and are in very good agreement with experiment for the lower Mach numbers. For higher Mach numbers in the vicinity of the transonic dip region, the inviscid codes become increasingly conservative. For this wing, inviscid calculations should not be used for $M > 0.80$.

2) For Mach numbers at and below the minimum transonic flutter speed index, the viscous methods, CAP-TSDV and CFL-3D, are in
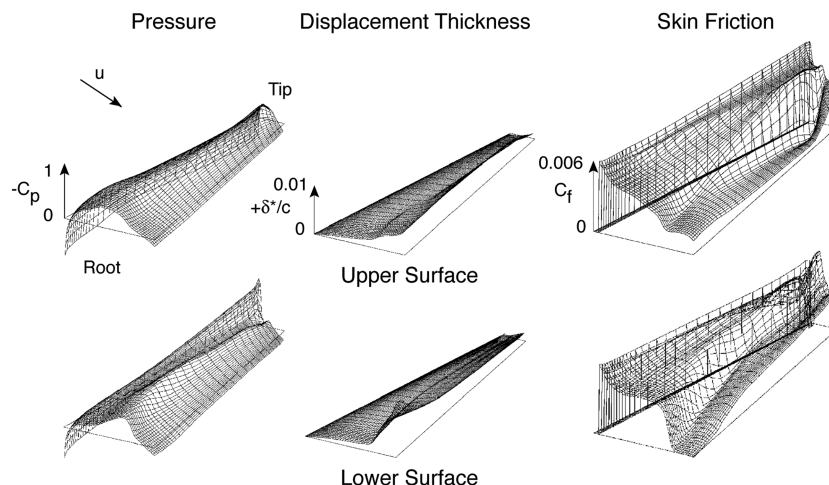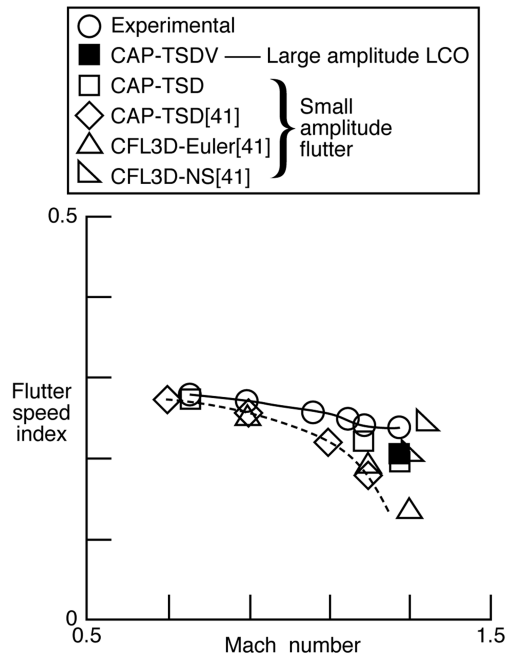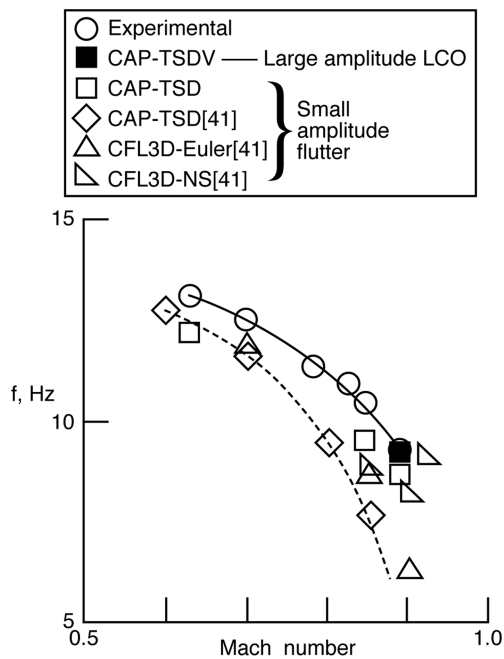

Fig. 12 Contour plots of transport wing pressure and boundary layer parameters at statically deformed conditions: $M = 0.888$, $Q = 79$ psf, $\alpha = 0.2$ deg, $\lambda_l = 1$, and $Re = 1.14 \times 10^6$.
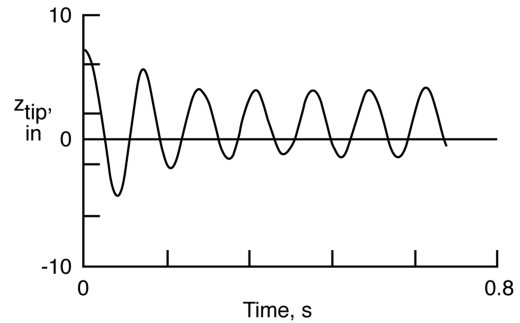
a) Flutter speed index

b) Frequency

Fig. 13   Comparison between experimental and calculated flutter speed index and frequency for a transport wing flutter model tested in air.

a) Amplitude decaying to limit cycle oscillation

b) Amplitude growing to limit cycle oscillation

Fig. 14   Calculated limit cycle response for a transport wing flutter model: $M = 0.888$, $Q = 79$ psi, $\lambda = 1$, and $Re = 1.14 \times 10^6$.
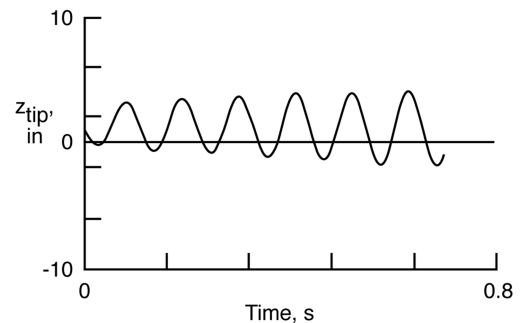
agreement and both provide good agreement with experiment, largely correcting the deficiency in the inviscid methods.

3) Linear flutter calculations [41] are in excellent agreement with experiment up to $M = 0.85$, but cannot be relied upon for higher transonic Mach numbers. The good agreement in the lower transonic speed range is due to well-known compensating defects of linear theory wherein thickness and viscous effects are neglected.

All of the results discussed thus far were obtained from transient responses of small amplitude, that is, wing tip response amplitudes were less than several tenths of an inch. Under these conditions, no large changes of the static aerodynamic loading occurred and transient responses exhibited exponential stability, characteristic of a "locally linear" system behavior. At $M = 0.888$ the CAP-TSDV code was able to calculate large amplitude response motions which demonstrated limit cycle behavior. The motion was calculated for the

experimental "flutter" dynamic pressure of 79 lb/ft^2. The conditions for the limit cycle are noted in Fig. 13 by the solid symbol indicating a 0.5 Hz increase in frequency over the small amplitude value. Figure 14 shows two transient responses confirming the limit cycle behavior. The motions were excited from converged statically deformed conditions by multiplying the modal displacements and velocities by factors of 5.0 for Fig. 14a and 0.5 for Fig. 14b. The larger factor simulates a wing tip displacement of about 7 in., resulting in decaying oscillations to a limit cycle with an amplitude of 5–6 in. peak to peak. The smaller factor results in oscillations growing in amplitude to the limit cycle. This behavior is similar to model behavior observed during the test. Video tape of the model motions at the experimental flutter conditions for this Mach number shows the model to be undergoing constant amplitude wing oscillations with amplitude of slightly less than one tip chord (6.3 in.) peak to peak. This is in very good agreement with the calculated LCO amplitude and frequency shown in Fig. 14. The author is unaware of other computations of transonic LCO with this relative amplitude of wing motion by any level of computational aeroelastic analysis code. The plate construction of the model provides sufficient strength to allow the model to sustain oscillations of this amplitude without structural failure. Inspection of the wing boundary layer parameters and surface pressures during the calculated limit cycle oscillations confirmed that the flow over the wing was intermittently separating and reattaching in the outboard upper and lower surface regions described above. This apparently provides the mechanism needed to quench the growth of the unstable flutter mode motions.

Effect of Reynolds number, $\lambda_l = 10$: A limited study of the effect of Reynolds number on this LCO behavior at $M = 0.888$ was conducted. Figure 15 shows the steady deformed wing pressure contours. Comparison with Fig. 12 indicates modest changes in the wing loading for the increased Reynolds number. Boundary layer parameters (not shown) indicate that the displacement thickness over the wing is approximately half that shown for $\lambda_l = 1$, accounting for the increased gradients seen in c_p in the inboard region of the lower surface and the outboard region of the upper surface in Fig. 15. The wing lift and moment coefficients decreased slightly from $C_L = 0.034$ and $C_M = -0.038$ for $\lambda_l = 1$ to $C_L = 0.017$ and $C_M = -0.027$ for $\lambda_l = 1$ and the scaled wing tip displacement decreased by several tenths of an inch.
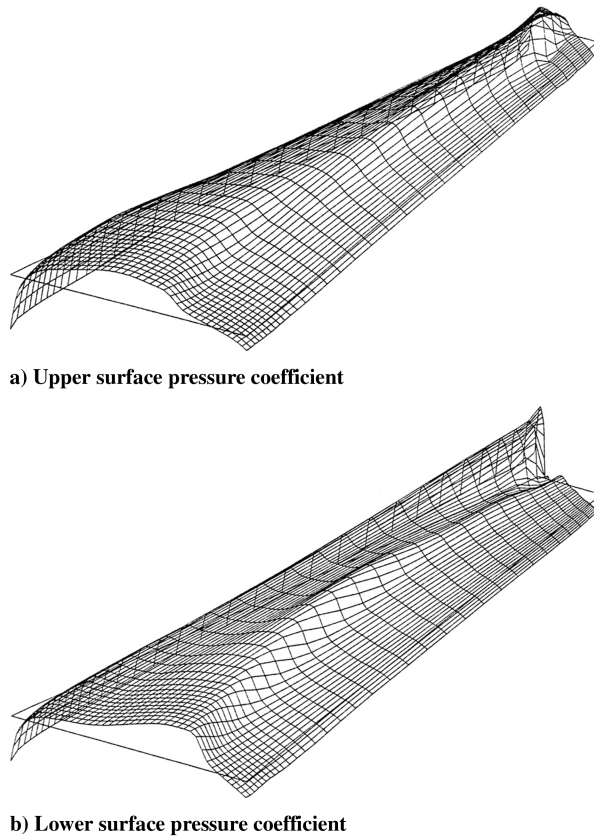
a) **Upper surface pressure coefficient**

b) **Lower surface pressure coefficient**

Fig. 15   Contour plots of transport wing pressure at statically deformed conditions: $M = 0.888$, $Q = 79$ psi, $a = 0.2$ deg, $\lambda_l = 10$,   and $Re = 11.4 \times 10^6$.
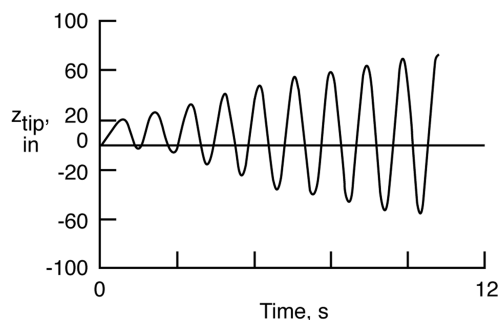

Fig. 16   Calculated limit cycle response for a transport wing flutter model: $M = 0.888$, $Q = 79$ psf, $\lambda_l = 10.0$, and $Re = 11.4 \times 10^6$.

Figure 16 shows the effect of the increased Reynolds number upon the LCO behavior of the wing. If there had been no effect, the wing oscillations would be expected to grow to a LCO condition with wing tip motions of about ±30 in., whereas the actual motion shown in Fig. 16 has reached ±60 in. and has not yet achieved stable limit cycle conditions. Although the higher Reynolds number leads to increased pressure gradients and hence slightly increased transonic shock strength, the thinner boundary layer is apparently less prone to providing the quenching mechanism for the LCO and larger wing motions are required to induce such quenching. In the present case, scaled LCO motions for the $\lambda_l = 10$ case are over twice the LCO motions calculated and observed for the wind-tunnel model scale which was tested. This might infer that the wind-tunnel flutter model test provided an unconservative flutter boundary. On the other hand, the large LCO motions observed during the test were correctly interpreted by the test engineers as flutter. The ambiguity underlying this discussion of stability for realistic flutter model testing should be interpreted as a requirement for an expanded concept of stability for transonic flutter computations and testing.

Conclusions

A viscous–inviscid interactive coupling method has been described, directed toward the computation of unsteady separating and reattaching transonic flows which must be treated in cases of self-excited shock-induced oscillations and transonic flutter. Lag-entrainment integral boundary layer equations and a transonic small-disturbance potential code are coupled with a variable gain, integral control coupling method.

Flutter calculations for the AGARD 445.6 flutter model are in excellent agreement with experiment for $M < 1.0$ for models tested in air and heavy gas. Calculations with the CAP-TSDV code are in excellent agreement with results from a Navier–Stokes code at $M = 0.96$. For Mach numbers below and very near unity, viscous modeling is required for such thin wings to achieve acceptable accuracy. In this region, calculations show evidence of small amplitude limit cycle behavior. Effects of scale and Reynolds number for this 4% thick model are small for Mach numbers less than the minimum transonic flutter speed, less than 1% decrease in flutter speed for increasing Reynolds number from 1 to 140×10^6. For Mach numbers just above the minimum transonic flutter speed, nonlinear amplitude effects are larger than Reynolds number effects for this wing. It is important to note that for this model and these test conditions, there are no strong transonic flow features or shocks and the flow is completely attached.

Flutter calculations for a transport wing model also show very good agreement with experiment for the available test data up to $M = 0.9$. For this thicker wing, the requirement for viscous modeling extends to lower transonic Mach numbers. Again, calculations with the CAP-TSDV code are in very good agreement with a Navier–Stokes code at $M = 0.888$ for small amplitude flutter motions. For large amplitude wing oscillations, the CAP-TSDV code predicts limit cycle behavior at this Mach number in very good agreement with that observed during wind-tunnel tests of the model. Also, the effect of a tenfold increase in scale or Reynolds number leads to a thinner boundary layer, weaker viscous effects, and limit cycle oscillation amplitude grows to over twice that which would be calculated from scaling of the observed wind-tunnel flutter model LCO amplitude.

Although these computational cases demonstrate a significant capability available with this viscous coupling methodology along with the CAP-TSD code, it is important to understand the limitations as well as the benefits that are involved. There are obvious limitations in the quasi-steady, two-dimensional, viscous boundary layer modeling. The viscous–inviscid coupling method enables computations for transonic shock-induced separation onset and mild penetration into separated flow regions. However, solutions in these regions are not strongly converged [34] and code failure can occur with increasing penetrations. On the other hand, the simplicity of the transonic small-disturbance potential equation and the lag-entrainment boundary layer equations provides significant benefits in efficiency which has been noted in [35–38]. Thus the CAP-TSDV code is a candidate as a conceptual design level analysis tool or as a screening tool for critical cases to be attacked with higher level computational aeroelasticity codes.

Acknowledgments

References

[1] Cunningham, A. M., "Practical Problems: Airplanes," *Unsteady Transonic Aerodynamics*, edited by D. Nixon AIAA Progress in

Aeronautics and Astronautics, AIAA, Washington, D.C., Vol. 120, Chap. 2, 1989.

[2] Mabey, D. G., "Physical Phenomena Associated with Unsteady Transonic Flow," *Unsteady Transonic Aerodynamics*, edited by D. Nixon, AIAA Progress in Aeronautics and Astronautics, AIAA, Washington, D.C., Vol. 120, Chap. 1, 1989.

[3] Eckstrom, C. V., Seidel, D. A., and Sandford, M. C., "Unsteady Pressure and Structural Response Measurements on an Elastic Supercritical Wing," AIAA Paper 88-2277, April 1988.

[4] McDevitt, J. B., "Supercritical Flow About a Thick Circular-Arc Airfoil," NASA TM-78549, Jan. 1979.

[5] McDevitt, J. B., Levy, L. L., Jr., and Deiwert, G. S., "Transonic Flow About a Thick Circular-Arc Airfoil," *AIAA Journal*, Vol. 14, May 1976, pp. 606–613.
doi:10.2514/3.61402

[6] McDevitt, J. B., and Okuno, A. F., "Static and Dynamic Pressure Measurements on a NACA 0012 Airfoil in the Ames High Reynolds Number Facility," NASA TP-2485, June 1985.

[7] Lee, B. H. K., "Oscillatory Shock Motion Caused by Transonic Shock Boundary-Layer Interaction," *AIAA Journal*, Vol. 28, No. 5, May 1990, pp. 942–944.
doi:10.2514/3.25144

[8] Hirose, N., and Miwa, H., "Computational and Experimental Research on Buffet Phenomena of Transonic Airfoils," NAL TR-996T, 1988.

[9] Edwards, J. W., and Thomas, J. L., "Computational Methods for Unsteady Transonic Flows," *Unsteady Transonic Aerodynamics*, edited by D. Nixon, AIAA Progress in Aeronautics and Astronautics, AIAA, Washington, D.C., Vol. 120, Chap. 5, 1989.

[10] Levy, L. L., Jr., "Experimental and Computational Steady and Unsteady Transonic Flows About a Thick Airfoil," *AIAA Journal*, Vol. 16, June 1978, pp. 564–572.
doi:10.2514/3.60935

[11] Rumsey, C. L., Sanetrik, M. D., Biedron, R. T., Melson, N. D., and Parlette, E. B., "Efficiency and Accuracy of Time-Accurate Turbulent Navier-Stokes Computations," AIAA Paper 95-1835, June 1995.

[12] Bartels, R. E., "Interactive Boundary Layer Computations Using the Improved k-ω Turbulence Model," *Proceedings Of the 9th International Conference on Numerical Methods in Laminar and Turbulent Flow*, Pineridge Press, Swansea, U.K., 1995.

[13] Bartels, R. E., and Rothmayer, A. P., "An IBL Approach to Multiscaled Shock Induced Oscillation," AIAA Paper 95-2157, June 1995.

[14] Edwards, J. W., and Malone, J. B., "Current Status of Computational Methods for Transonic Unsteady Aerodynamic and Aeroelastic Applications," Paper No. 1, Transonic Unsteady Aerodynamics and Aeroelasticity, AGARD CP 507, March 1992.

[15] Edwards, J. W., "Technical Evaluation Report on 1991 Specialists' Meeting on Transonic Unsteady Aerodynamics and Aeroelasticity," Paper T, Transonic Unsteady Aerodynamics and Aeroelasticity, AGARD CP 507, March 1992.

[16] Green, J. E., Weeks, D. J., and Brooman, J. W. F., "Prediction of Turbulent Boundary Layers and Wakes in Compressible Flow by a Lag-Entrainment Method," British Aeronautical Research Council, R & M No. 3791, 1977.

[17] Carter, J. E., "A New Boundary-Layer Inviscid Iteration Technique for Separated Flows," AIAA Paper 79-1450, July 1979.

[18] Melnik, R. E., and Brook, J. W., "The Computation of Viscid/Inviscid Interaction on Airfoils With Separated Flow," *Third Symposium on Numerical and Physical Aspects of Aerodynamic Flows*, California State University, Long Beach, CA, 1985, pp. 1-21–1-37.

[19] LeBalleur, J. C., and Girodroux-Lavigne, P., "A Viscous-Inviscid Interaction Method for Computing Unsteady Transonic Separation," *Third Symposium on Numerical and Physical Aspects of Aerodynamic Flows*, California State University, Long Beach, CA, 1985 (ONERA T. P. No. 1985-5).

[20] Houwink, R., and Veldman, A. E. P., "Steady and Unsteady Separated Flow Computations for Transonic Airfoils," AIAA Paper 84-1618, June 1984.

[21] Houwink, R., "Computation of Unsteady Turbulent Boundary Layer Effects on Unsteady Flow About Airfoils," *Fourth Symposium on Numerical and Physical Aspects of Aerodynamic Flows*, California State University, Long Beach, CA, Jan. 1989; also NLR TP 89003 U, 1989.

[22] Thomas, J. L., "Transonic Viscous-Inviscid Interaction Using Euler and Inverse Boundary-Layer Equations," Ph.D. Thesis, Mississippi State Univ., Mississippi State, MS, Dec. 1983.

[23] Edwards, J. W., "Transonic Shock Oscillations Calculated with a New Interactive Boundary Layer Coupling Method," AIAA Paper 93-0777, Jan. 1993.

[24] Holst, T. L., "Viscous Transonic Airfoil Workshop Compendium of Results," *Journal of Aircraft*, Vol. 25, Dec. 1988, pp. 1073–1087.
doi:10.2514/3.45706

[25] Chang, K. C., Alemdaroğula, N., Mehta, U., and Cebeci, T., "Further Comparisons of Interactive Boundary-Layer and Thin-Layer Navier-Stokes Procedures," *Journal of Aircraft*, Vol. 25, Oct. 1988, pp. 897–903.
doi:10.2514/3.45677

[26] Drela, M., and Giles, M. B., "Viscous-Inviscid Analysis of Transonic and Low Reynolds Number Airfoils," *AIAA Journal*, Vol. 25, Oct. 1987, pp. 1347–1355.
doi:10.2514/3.9789

[27] Fenno, C. C., Jr., Newman, P. A., and Hassan, H. A., "Unsteady Viscous-Inviscid Interaction Procedures for Transonic Airfoils Using Cartesian Grids," *Journal of Aircraft*, Vol. 26, Aug. 1989, pp. 723–730.
doi:10.2514/3.45831

[28] Kusunose, K., Wigton, L., and Meredith, P., "A Rapidly Converging Viscous/Inviscid Code for Multi-Element Airfoil Configurations," AIAA Paper 91-0177, Jan. 1991.

[29] Howlett, J. T., "Efficient Self-Consistent Viscous Inviscid Solution for Unsteady Transonic Flow," *Journal of Aircraft*, Vol. 24, Nov. 1987, pp. 737–744.
doi:10.2514/3.45515

[30] Howlett, J. T., "Calculation of Unsteady Transonic Flows With Mild Separation by Viscous-Inviscid Interaction," NASA TP-3197, June 1992.

[31] Rizzetta, D. P., "Procedures for the Computation of Unsteady Transonic Flows Including Viscous Effects," NASA CR-155249, Jan. 1982.

[32] Batina, J. T., "Unsteady Transonic Algorithm Improvements for Realistic Aircraft Configurations," *Journal of Aircraft*, Vol. 26, Feb. 1989, pp. 131–139.
doi:10.2514/3.45734

[33] Batina, J. T., "A Finite-Difference Approximate- Factorization Algorithm for Solution of the Unsteady Transonic Small-Disturbance Equation," NASA TP 3 129, Jan. 1992.

[34] Edwards, J. W., "Transonic Shock Oscillations and Wing Flutter Calculated with an Interactive Boundary Layer Coupling Method," NASA TM 110284, Aug. 1996.

[35] Dreim, D. R., Jacobson, S. B., and Britt, R. T., "Simulation of Nonlinear Transonic Aeroelastic Behavior on the B-2," *Proceedings of the CEAS/AIAA/ICASE/NASA Longley International Forum on Aeroelasticity and Structural Dynamics*, NASA Langley Research Center, Hampton, VA, 1999, p. 511.

[36] Huttsell, L., Schuster, D., Volk, J., Giesing, J., and Mike Love, M., "Evaluation of Computational Aeroelasticity Codes for Loads and Flutter," AIAA Paper 2001-569, 8–11 Jan. 2001.

[37] Beran, P. S., Khot, N. S., Eastep, F. E., Snyder, R. D., and Zweber, J. V., "Numerical Analysis of Store-Induced Limit-Cycle Oscillation," *Journal of Aircraft*, Vol. 41, No. 6, Nov.–Dec. 2004, pp. 1315–1326.
doi:10.2514/1.404

[38] Denegri, C. M., Jr., and Dubben, J. A., "F-16 Limit Cycle Oscillation Analysis Using Transonic Small-Disturbance Theory," AIAA Paper 2005-2296, 2005.

[39] Bendiksen, O. O., "Transonic Limit Cycle Flutter/LCO," AIAA Paper 2004-2694, 2004.

[40] Thomas, J. P., Dowell, E. H., Hall, K. C., and Denegri, C. M., Jr., "Modeling Limit Cycle Oscillation Behavior of the F-16 Fighter Using a Harmonic Balance Approach," AIAA Paper 2004-1696, 2004.

[41] Gibbons, M. D., "Aeroelastic Calculations Using CFD for a Typical Business Jet Model," NASA CR 4753, Sept. 1996.

[42] Batina, J. T., "Unsteady Transonic Small-Disturbance Theory Including Entropy and Vorticity Effects," *Journal of Aircraft*, Vol. 26, June 1989, pp. 531–538.
doi:10.2514/3.45799

[43] Regier, A. A., "The Use of Scaled Dynamic Models in Several Aerospace Vehicle Studies," *Colloquium on the Use of Models and Scaling in Shock and Vibration*, Winter Annual Meeting of the ASME, American Society of Mechanical Engineers, Fairfield, NJ, 19 Nov. 1963.

[44] Dupriex, F., "Flutter Models, Their Design, Manufacture, and Ground Testing," von Karman Institute for Fluid Dynamics Lecture Series 1992-01, Introduction to Flutter of Winged Aircraft, 9–13 Dec. 1991.

[45] Yates, E. C. Jr., "AGARD Standard Aeroelastic Configurations for Dynamic Response. Candidate Configuration I.—Wig 445.6," NASA TM 100492, Aug. 1987.

[46] Yates, E. C., Jr., Land, N. S., and Foughner, J. T., Jr., "Measured and Calculated Subsonic and Transonic Flutter Characteristics of a 45 Degree Sweptback Wig Planform in Air and in Freon-12 in the Langley Transonic Dynamics Tunnel," NASA TN D-1616, March 1963.